INTERNATIONAL JOURNAL FOR NUMERICAL METHODS IN FLUIDS
Int. J. Numer. Meth. Fluids 2002; **38**:71–98 (DOI: 10.1002/fld.207)

A fully coupled numerical technique for 2D bed morphology calculations

Johannes V. Soulis*

Fluid Mechanics/Hydraulics Division, Department of Civil Engineering, Democrition University of Thrace, Xanthi 67100, Greece

SUMMARY

A fully coupled two-dimensional subcritical and/or supercritical, viscous, free-surface flow numerical model is developed to calculate bed variations in alluvial channels. Vertically averaged free-surface flow equations in conjunction with sediment transport equation are numerically solved using an explicit finite-volume scheme using transformed grid in order to handle complex geometry fluvial problems. Convergence is accelerated with use of a multi-grid technique. Firstly the capabilities of the proposed method are demonstrated by analyzing subcritical and supercritical hydrodynamic flows. Thereafter, an analysis of one- and two-dimensional flows is performed referring to aggradation and scouring. For all reported test cases the computed results compare reasonably well with measurements as well as with other numerical solutions. The method is stable, reliable and accurate handling a variety of sediment transport equations with rapid changes of sediment transport at the boundaries. Copyright © 2002 John Wiley & Sons, Ltd.

KEY WORDS: bed morphology; aggradation; scouring; viscous flow; fully coupled; depth-averaged; finite-volume scheme

1. INTRODUCTION

In recent years significant advances have been made in computational fluid dynamics (CFD) applied to alluvial channels. Scour and deposition in alluvial channels is provoked by the removal of bed material due to flowing water thus the formation and the evolution of such channels is governed by the interaction between flow dynamics and morphological response of the mobile bed. The flow pattern of the aforementioned region is highly complex. This complexity increases as the scouring increases. Moreover, the accurate quantitative estimation of scour and deposition in alluvial channels is of paramount importance in river control engineering or in predicting the water surface elevations during floods. During these floods, bridge failures due to local scour of the bed of the river at the nearby regions of piers and abutments, is usual. Knowledge of the process of development of such scouring and

*Correspondence to: J. V. Soulis, Fluid Mechanics/Hydraulics Division, Department of Civil Engineering, Democrition University of Thrace, Xanthi 67100, Greece.

Received July 2000
Revised March 2001

deposition, the time necessary to reach the equilibrium state and the maximum depth of scour are important to protect the hydraulic structures.

The free-surface flow in the vicinity of hydraulic structures such as bridge piers or abutments is fully three-dimensional. Methodologies for the estimation of bed morphology may be developed through the application of three-dimensional hydrodynamic models coupled to sediment transport models. However, fully coupling the three-dimensional hydrodynamic equations with sediment transport is still a formidable task. The scour around a circular pile exposed to a steady current using a 3D numerical model incorporated with κ-ω, *shear stress transport* (SST) closure (*EllipSys3D program*) coupled with sediment-continuity equation and a bedload sediment transport formula has been used by Roulund *et al.* [1] to predict the scour. They report fairly good agreement with experimental data. This approach was explored by Olsen and Melaaen [2] to simulate the growth of the scour hole in the base of a circular pier. Further verification of the flow field, which constitutes the basis of the scouring mechanism, was needed. Richardson and Panchang [3], simulated the flow occurring at the base of a cylindrical bridge pier within a scour hole using a fully three-dimensional hydrodynamic model (*FLOW-3D*). They report that quantitative and qualitative agreement between the studies was quite good. For two-dimensional (depth-averaged) applications a number of investigators report uncoupled, semi-coupled and fully coupled numerical techniques. Among them, Struiksma *et al.* [4], analyzed bed deformation in curved alluvial channels using a two-dimensional semi-coupled model. Good agreement with the experimental data was reported. Kassem and Chaudhry [5] compared a 2D fully coupled model with a semi-coupled one using the well known Beam and Warming alternative-direction implicit scheme to calculate bed variations in alluvial channels. Computed results compared satisfactorily with experimental results obtained in a laboratory flume. Numerous publications are reported for one-dimensional bed deformation in alluvial channels, amongst them Bhallamudi and Chaudhry [6], Klonidis and Soulis [7], Farsirotou *et al.* [8] and others. A review of the state of the art is given in DeVries *et al.* [9].

The objective of this research work is to investigate the bed formation in alluvial channels as well as in regions around bridge piers and abutments using a stable, reliable and accurate depth-averaged numerical approach. For this purpose a fully coupled hydrodynamic-sediment transport model is developed. The fully coupled model is the method employed to achieve solution. Fully coupled models use the current values of flow and sediment variables, which have mutual interaction. The flow equations are solved along with the sediment transport equation simultaneously in a given time step. In the uncoupled approach, flow and bed topography are treated separately in each time step, during which the bed level is kept unchanged for flow simulation. To achieve solution a viscous, explicit, finite-volume multi-grid numerical procedure using transformed grid is incorporated. The method is an explicit numerical technique requiring substantial computational time to achieve solution. However, it is in favor of an implicit technique as far as the programming complexity is concerned. In an explicit numerical technique the required CPU time per iteration is small compared to the CPU time per iteration of an implicit technique. The implicit schemes permit numerical solutions over large time steps. Overall, an implicit technique is substantially faster to the explicit one.

This paper is an extension and improvement of previous research work on inviscid (it was assumed that the resistance is due to bottom and bank friction), steady, depth-averaged, subcritical and supercritical flow for open channel calculations developed by Soulis [10]. First, the hydrodynamic model is verified under subcritical and supercritical two-dimensional flow,

thereafter the validation of the proposed model is performed solving problems of aggradation (one-dimensional flow) and around abutments (two-dimensional). The bed morphology predictions are compared with measurements as well as with computed results using other numerical techniques. With the bed-evolution equation and the time-scale parameter obtained, it is possible to estimate scour depth and deposition height under different flow conditions at various times and locations.

2. HYDRODYNAMIC AND BED MORPHOLOGY EQUATIONS

The governing flow equations for the physical domain, assuming the flow to be homogeneous, incompressible, two-dimensional, viscous with a hydrostatic pressure distribution along the vertical in channels with a movable bed, is described by a system of non-linear, partial differential equations. In the absence of wind stresses at the water surface and Coriolis forces these equations are written as,

$$E_t + F_x + G_y = Q \tag{1}$$

where the variables E, F, G and Q are defined in matrix form as follows,

$$E = \begin{bmatrix} h \\ hu \\ hv \\ (1-p)z_b \end{bmatrix}, \qquad F = \begin{bmatrix} hu \\ hu^2 + gh^2/2 - \nu_{\text{eff}}\left[2\dfrac{\partial(hu)}{\partial x}\right] \\ huv - \nu_{\text{eff}}\left[\dfrac{\partial(hu)}{\partial y} + \dfrac{\partial(hv)}{\partial x}\right] \\ q_{sx} \end{bmatrix}$$

$$G = \begin{bmatrix} hv \\ huv - \nu_{\text{eff}}\left[\dfrac{\partial(hu)}{\partial y} + \dfrac{\partial(hv)}{\partial x}\right] \\ hv^2 + gh^2/2 - \nu_{\text{eff}}\left[2\dfrac{\partial(hv)}{\partial y}\right] \\ q_{sy} \end{bmatrix}, \qquad Q = \begin{bmatrix} 0 \\ gh(S_{0x} - S_{fx}) \\ gh(S_{0y} - S_{fy}) \\ 0 \end{bmatrix} \tag{2}$$

Here x and y represent the Cartesian coordinate positions in the longitudinal and transverse directions respectively; t is the time; u and v are the depth-averaged velocity components in the x and y directions; h is the water depth; g is the gravity acceleration; ν_{eff} is the effective kinematic viscosity, z_b is the bed elevation, p is the sediment porosity, q_{sx} and q_{sy} are the sediment discharge per unit width in the x and y directions, $S_{0x} = [(-\partial z_b)/(\partial x)]$ and $S_{0y} = [(-\partial z_b)/(\partial y)]$ are the channel slopes and S_{fx} and S_{fy} are the friction slopes which are defined as,

$$S_{fx} = \frac{n^2 u\sqrt{u^2+v^2}}{h^{4/3}} \quad \text{and} \quad S_{fy} = \frac{n^2 v\sqrt{u^2+v^2}}{h^{4/3}} \tag{3}$$

where n is the Manning's flow friction coefficient. Another option utilizes the Chezy's flow friction formula. Changes in bed level, due to longitudinal and transverse imbalances in sediment discharge, are obtained based on numerical solution of continuity equations for sediment in the respective directions. By writing the equation for frictional resistance in this way it was assumed that the resistance is due to bottom friction. The depth-integrated effective stress has been neglected in order to eliminate the possibility of introducing numerical smoothing. Friction losses in unsteady flow are not significantly different from those in the steady flow. For all reported applications the effective kinematic viscosity v_{eff} is defined as,

$$v_{\text{eff}} = \frac{g}{C^2} h \sqrt{(u^2 + v^2)} \tag{4}$$

where $C = [(h^{1/6})/n]$ is the Chezy's, friction coefficient for flow. The sediment discharge may be predicted by one of the following bed-load formulae available in the present model:

(a) empirical power function of the flow velocity, Soni *et al.* [11].
(b) Ackers and White [12].
(c) Engelund and Hansen [13].
(d) Brownlie [14].
(e) Smart [15].

Therefore, some empirical relations have to be used to relate local velocity with local shear stress and the latter with sediment flow rate. The reliability of the model is strictly dependent upon the accuracy of the semi-empirical equations used to evaluate the sediment transport. There is no solid transport formula valid for all ranges of natural conditions.

3. TRANSFORMATION OF THE UNSTEADY FLOW EQUATIONS

In order to overcome the difficulties and inaccuracies associated with the determination of flow characteristics near the flow boundaries as well as to have the ability to use dense or sparse computational grid points in predefined flow regions, the governing system of partial differential equations, i.e. Equation (1), are transformed into an equivalent system applied over a square grid network. Thus, the essence of the presented numerical scheme is that quadrilaterals in the physical domain will be separately mapped into squares, subsequently called finite-volumes, in the computational domain by independent transformations from global (x, y) to local (ξ, η) coordinates. Linear shape functions are defined in terms of a non-orthogonal coordinate system (ξ, η) for the quadrilaterals. Let H be the transformation matrix from the physical system to the computational, then,

$$H = \begin{bmatrix} x_\xi & x_\eta \\ y_\xi & y_\eta \end{bmatrix} \tag{5}$$

with

$$J^{-1} = [H] \tag{6}$$

The following relations hold [10],

$$x_\xi = J^{-1}\eta_y, \quad x_\eta = -J^{-1}\xi_y, \quad y_\xi = -J^{-1}\eta_x, \quad y_\eta = J^{-1}\xi_x \tag{7}$$

Under the aforementioned transformation of Equation (1) in the local co-ordinate system (ξ, η) they assume the form,

$$E'_t + F'_\xi + G'_\eta = D' \tag{8}$$

where

$$E' = J^{-1}\begin{bmatrix} h \\ hu \\ hv \\ (1-p)z_b \end{bmatrix}$$

$$F' = J^{-1}\begin{bmatrix} hU \\ hUu + \xi_x gh^2/2 - \nu_{\text{eff}}\left[\xi_x 2\dfrac{\partial(hu)}{\partial x} + \xi_y\left(\dfrac{\partial(hu)}{\partial y} + \dfrac{\partial(hv)}{\partial x}\right)\right] \\ hUv + \xi_y gh^2/2 - \nu_{\text{eff}}\left[\xi_x\left(\dfrac{\partial(hu)}{\partial y} + \dfrac{\partial(hv)}{\partial x}\right) + \xi_y 2\dfrac{\partial(hv)}{\partial y}\right] \\ Q_{s\xi} \end{bmatrix}$$

$$G' = J^{-1}\begin{bmatrix} hV \\ hVu + \eta_x gh^2/2 - \nu_{\text{eff}}\left[\eta_x 2\dfrac{\partial(hu)}{\partial x} + \eta_y\left(\dfrac{\partial(hu)}{\partial y} + \dfrac{\partial(hv)}{\partial x}\right)\right] \\ hVv + \eta_y gh^2/2 - \nu_{\text{eff}}\left[\eta_x\left(\dfrac{\partial(hu)}{\partial y} + \dfrac{\partial(hv)}{\partial x}\right) + \eta_y 2\dfrac{\partial(hv)}{\partial y}\right] \\ Q_{s\eta} \end{bmatrix} \tag{9}$$

$$Q' = J^{-1}\begin{bmatrix} 0 \\ gh(S_{0x} - S_{fx}) \\ gh(S_{0y} - S_{fy}) \\ 0 \end{bmatrix}$$

also $U, V, Q_{s\xi}$, and $Q_{s\eta}$ are velocity and transport components along ξ and η directions, respectively. The following equations hold,

$$\begin{bmatrix} u \\ v \end{bmatrix} = J^{-1}\begin{bmatrix} U \\ V \end{bmatrix}, \quad \begin{bmatrix} q_{sx} \\ q_{sy} \end{bmatrix} = J^{-1}\begin{bmatrix} Q_{s\xi} \\ Q_{s\eta} \end{bmatrix} \tag{10}$$

4. NUMERICAL SOLUTION PROCEDURE

4.1. Flow discretization

The 2D, depth-averaged unsteady flow equations are numerically solved using a 'time-marching' explicit scheme. This scheme has been extensively used to solve the 2D, compressible Navier–Stokes equations. Since the governing flow equations are solved in conservative form, the scheme is 'shock-capturing'. A major improvement was obtained by solving the above flow and sediment equations in integral form, i.e. by applying the equations of continuity, ξ-momentum, η-momentum and sediment to a series of finite-volumes with adjacent volumes sharing a common face. At the end of each time step Δt the net flux into each elemental volume is zero, so that overall water mass flow and sediment transport are conserved and the changes in momentum are equal to the forces imposed by the boundaries of the system. The two-dimensional flow and sediment equations may be written as conservation equations for a control volume ΔV of unit height and for a time step Δt as,

$$-\Delta(J^{-1}h) = [\Delta(J^{-1}hU)\Delta\eta + \Delta(J^{-1}hV)\Delta\xi]\frac{\Delta t}{\Delta\xi\Delta\eta} \tag{11}$$

$$-\Delta(J^{-1}hu) = \left\{\begin{array}{l} \Delta\left[J^{-1}\left(hUu + \xi_x\left(gh^2/2 - 2v_{\text{eff}}\dfrac{\partial(hu)}{\partial x}\right)\right.\right. \\ \qquad \left.\left. -\xi_y v_{\text{eff}}\left(\dfrac{\partial(hu)}{\partial y} + \dfrac{\partial(hv)}{\partial x}\right)\right)\right]\Delta\eta + \\ \Delta\left[J^{-1}\left(hVu + \eta_x\left(gh^2/2 - 2v_{\text{eff}}\dfrac{\partial(hu)}{\partial x}\right)\right.\right. \\ \qquad \left.\left. -\eta_y v_{\text{eff}}\left(\dfrac{\partial(hu)}{\partial y} + \dfrac{\partial(hv)}{\partial x}\right)\right)\right]\Delta\xi \end{array}\right\}\frac{\Delta t}{\Delta\xi\Delta\eta} \tag{12}$$

$$-\Delta(J^{-1}hv) = \left\{\begin{array}{l} \Delta\left[J^{-1}\left(hUv + \xi_y\left(gh^2/2 - 2v_{\text{eff}}\dfrac{\partial(hv)}{\partial y}\right)\right.\right. \\ \qquad \left.\left. -\xi_x v_{\text{eff}}\left(\dfrac{\partial(hu)}{\partial y} + \dfrac{\partial(hv)}{\partial x}\right)\right)\right]\Delta\eta + \\ \Delta\left[J^{-1}\left(hVv + \eta_y\left(gh^2/2 - 2v_{\text{eff}}\dfrac{\partial(hv)}{\partial y}\right)\right.\right. \\ \qquad \left.\left. -\eta_x v_{\text{eff}}\left(\dfrac{\partial(hu)}{\partial y} + \dfrac{\partial(hv)}{\partial x}\right)\right)\right]\Delta\xi \end{array}\right\}\frac{\Delta t}{\Delta\xi\Delta\eta} \tag{13}$$

$$-\Delta[J^{-1}(1-p)z_{\text{b}}] = [\Delta(J^{-1}hQ_{s\xi})\Delta\eta + \Delta(J^{-1}hQ_{s\eta})\Delta\xi]\frac{\Delta t}{\Delta\xi\Delta\eta} \tag{14}$$

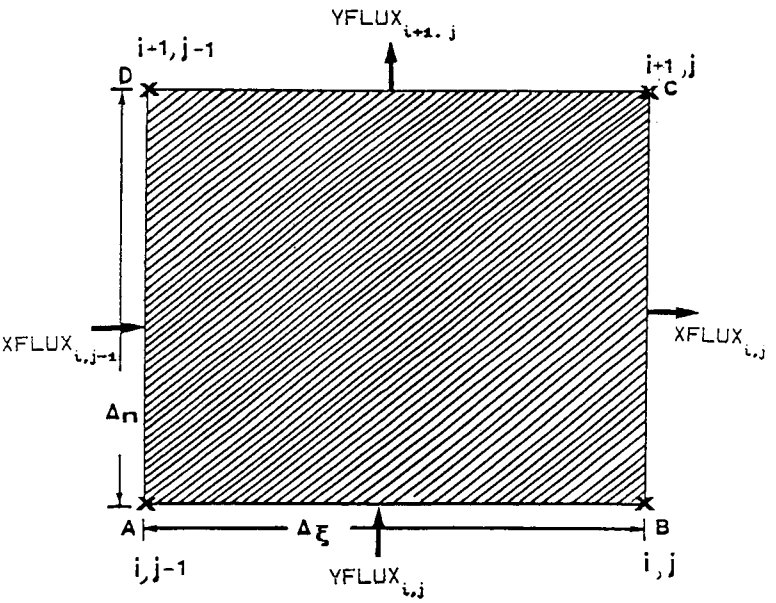

Figure 1. Notation for the mass flux balancing across a finite volume (cell).

Figure 1 shows the notation used for mass flux balancing across a finite-volume of the flow. Similar notation is adopted for the balancing of the ξ-momentum, η-momentum and sediment fluxes. Thus, for the water mass flux, an XFLUX at a point i, j is defined as,

$$(\mathrm{XFLUX})_{i,j} = [(J^{-1}hU)_{i+1,j} + (J^{-1}hU)_{i,j}]\,\frac{\Delta\eta}{2} \tag{15}$$

while the YFLUX, at the same point i, j, is defined as,

$$(\mathrm{YFLUX})_{i,j} = [(J^{-1}hV)_{i,j} + (J^{-1}hV)_{i,j-1}]\,\frac{\Delta\xi}{2} \tag{16}$$

The terms $\Delta(hu)$ and $\Delta(hv)$ of Equation (11) are defined as,

$$\Delta(J^{-1}hU) = (\mathrm{XFLUX})_{i,j} - (\mathrm{XFLUX})_{i,j-1} \tag{17}$$

$$\Delta(J^{-1}hV) = (\mathrm{YFLUX})_{i+1,j} - (\mathrm{YFLUX})_{i,j} \tag{18}$$

For the ξ-momentum, η-momentum and sediment transport flux balance, corresponding $(\mathrm{XFLUX})_{i,j}$ and $(\mathrm{YFLUX})_{i,j}$ values are developed. Similar differences are applied to all Δ terms of Equations (12), (13) and (14). The slopes S_{0x} and S_{0y} are pre-calculated and stored at the beginning of each time step, while the friction slopes S_{fx} and S_{fy} are updated continuously. For all bed and friction slopes averaged values of the appropriate physical quantities are used. The changes $\Delta(J^{-1}h)$, $\Delta(J^{-1}hu)$, $\Delta(J^{-1}hv)$, and $\Delta(J^{-1}z_b)$ are distributed between the four corners A, B, C and D of the finite-volume. Also, and this is crucial in achieving

convergence, the water depth is calculated using the current finite-volume involved and the downstream one according to,

$$h_{i,j}^{n+1} = 0.6h_{i,j}^{n+1} + 0.4\,h_{i,j+1}^{n+1} \tag{19}$$

where $n+1$ is the current iteration. The decision was made after numerical experimentation while the edges of the domain are not altered. The calculated changes $\Delta(J^{-1}h)$, $\Delta(J^{-1}hu)$, $\Delta(J^{-1}hv)$, and $\Delta(J^{-1}z_b)$ were not directly used to yield the h, hu, hv and z_b values. For all test runs and in order to stabilize the solution a C_1 factor is used for the h and z_b calculations and a C_2 factor for the hu and hv calculations. The procedure for the h (or z_b) and hu (or hv) calculation is as follows,

$$h_{i,j}^{n+1} = h_{i,j}^{n} + \frac{\Delta h_{i,j}^{n+1}}{1 + \frac{C_1}{h_{1,1}^{0}}\Delta h_{i,j}^{n+1}} \tag{20}$$

$$(hu)_{i,j}^{n+1} = (hu)_{i,j}^{n} + \frac{\Delta(hu)_{i,j}^{n+1}}{1 + \frac{C_2}{(hu)_{1,1}^{0}}\Delta(hu)_{i,j}^{n+1}} \tag{21}$$

where C_1 is typically equal to 0.1 and C_2 is 0.025. The upper index 0 denotes initial value. The numerical scheme was found to be stable over a wide range of C_1 and C_2 values. Two spatial smoothing factors operating on longitudinal and tangential flow directions were found necessary to be applied in order to maintain numerical stability. The applied smoothing equations are,

$$D_{i,j} = (1.0 - Sm_\xi)D_{i,j} + Sm_\xi(D_{i,j-1} + D_{i,j+1})/2 \tag{22}$$

$$D_{i,j} = (1.0 - Sm_\eta)D_{i,j} + Sm_\eta(D_{i-1,j} + D_{i+1,j})/2 \tag{23}$$

Sm_ξ and Sm_η being smoothing factors in ξ and η directions, respectively while D stands for any of the h, hu, hv and z_b. Typical value for either of the smoothing factors is close to 0.0005. This value is determined after numerical experimentation. The smoothing is performed in all iteration steps by keeping the D value fixed at its initial value of the under consideration time step Δt. The applied inlet and outlet flow conditions are not smoothed.

Computational grid formation requires minimum data. Grid nodes need not be uniformly spaced in any direction. Flow problems with large gradients of the physical quantities need dense computational grid formation for efficient flow depiction. Then, rather than using a uniform grid distribution in the tangential direction, grid points may be clustered in high flow gradients regions. This reduces the total amount of required grid points.

4.2. The iterative scheme

The full system of algebraic Equations (11)–(14) together with the specified boundary and initial conditions, constitutes a closed system of equations that can be solved for all computational points for every time step Δt during the period of computation. Firstly, the geometrical and physical data are read. The computational grid is then formed. From the initial bed elevation z_b, the initial bottom slopes of the channel are formed. To start the iterations a guessed linear distribution of the $gh^2/2$ quantity between inlet and outlet flow boundaries was assumed

and the u, v velocity components, the water depth h as well as the per unit sediment discharges q_{sx} and q_{sy} are calculated.

The iterations start by solving the water mass flux Equation (11), to obtain h^{n+1} using old values of u^n, v^n and h^n and a corrected water depth is obtained using Equation (20). Appropriate boundary flow conditions are applied at inlet and outlet flow. Equations (12) and (13) are solved to obtain $(hu)^{n+1}$ and $(hv)^{n+1}$ and thereby a new value for u^{n+1} and v^{n+1} is derived. The appropriate bed load formula is applied and the unit sediment discharges q_{sx} and q_{sy} are determined. The bed elevation Equation (14) is then solved to obtain z_b^{n+1}.

Solid boundary conditions are applied requiring no water or sediment flow to cross perpendicular to the solid surface. Also, smoothing factors are applied to the all changes of the flow field quantities. All these changes are sent to the appropriate nodes of the finite-volume involved. Finally, two convergence criteria are used and if they are not satisfied then the iterations continue. These criteria require that (a) the averaged over the flow field relative error based on the axial velocity component drops below 10^{-6} between successive iterations and (b) the average change in sediment transport also drops below 10^{-6} between successive iterations. The total number of iterations required to achieve convergence strongly depends on the actual time. For the first few time steps this number was of the order of 30 or so, depending of course upon the geometrical complexity, flow discharges and the time step used. In some cases it was found necessary, due to local errors, to enforce an upper limit concerning the iterations within the time step Δt, typically 50. As with all time-stepping methods the theoretical maximum stable time step Δt is specified according to the Courant–Friedrichs–Lewy (CFL) criterion,

$$\Delta t \leqslant \left\{ \min \left(\frac{\Delta x}{u_{i,j} + \sqrt{g h_{i,j}}}, \frac{\Delta y}{v_{i,j} + \sqrt{g h_{i,j}}} \right) \right\} \mathrm{FT} \tag{24}$$

where $\Delta x = x_{i,j} - x_{i,j-1}$ and $\Delta y = y_{i+1,j} - y_{i,j}$. FT is a constant determined after numerical experimentation. Typical values of it are less than unity. The converged solution, at any given time step, forms the initial condition for the next time step. Grid reduction tests have shown that the grid size, i.e. the ratio of Δx to Δy, does not affect the accuracy of the solution. However, for extreme $\Delta x/\Delta y$ ratios the solution does break down.

4.3. The multi-grid method

In the multi-grid application the corrections to fine grid points are transferred to a coarse grid to maintain the low truncation errors associated with fine level of discretizations. The solution is advanced simultaneously on the coarse and on the fine-grid. The coarse grid is constructed by combining a group of finite-volumes into a block. At the end of every time step the changes Δh, $\Delta(hu)$, $\Delta(hv)$ and Δz_b defined by Equations (11), (12), (13) and (14) respectively, are known for each finite-volume of the fine grid mesh. The changes of the block can be found by summing the already calculated changes for the finite-volumes within the block. In a typical 2×2 multi-grid, where the block of finite-volumes is $\mathrm{IMG} \times \mathrm{JMG} = 2 \times 2$

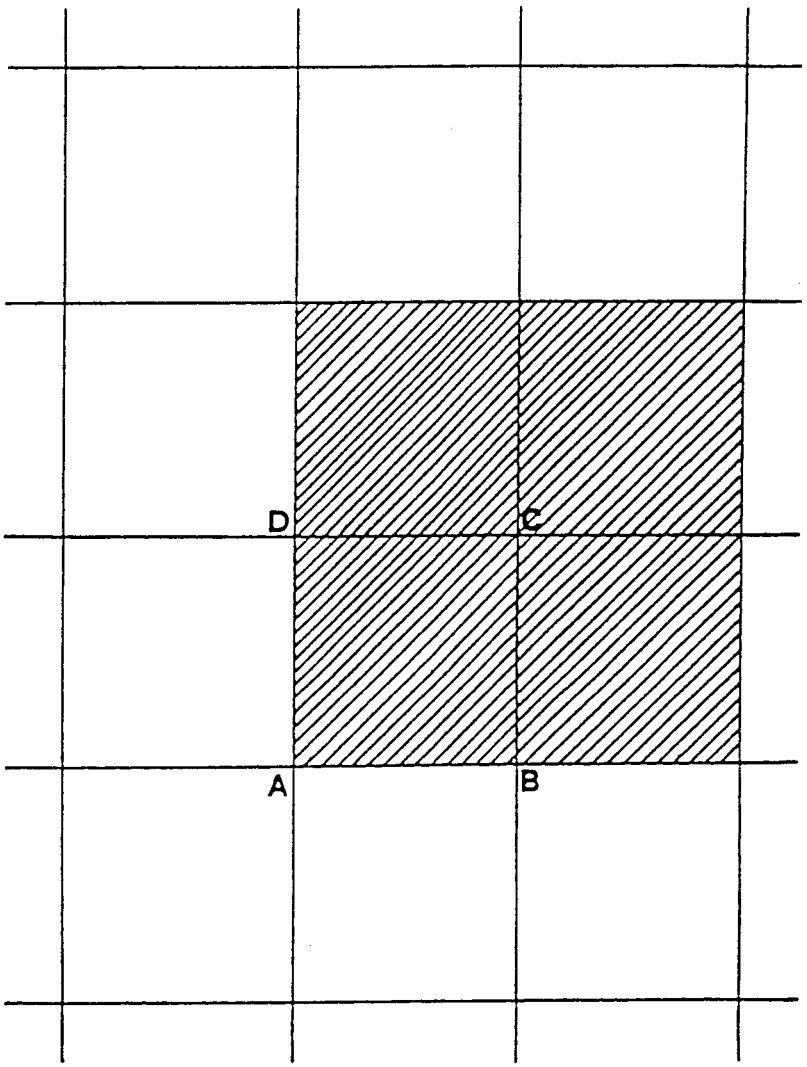

Figure 2. A 2×2 block size grid.

(see Figure 2) the values for the block Δh, $\Delta(hu)$, $\Delta(hv)$ and Δz_b are determined as follows,

$$\begin{aligned} \Delta h_{2\times 2} &= \Delta h_1 + \Delta h_2 + \Delta h_3 + \Delta h_4 \\ \Delta(hu)_{2\times 2} &= \Delta(hu)_1 + \Delta(hu)_2 + \Delta(hu)_3 + \Delta(hu)_4 \\ \Delta(hv)_{2\times 2} &= \Delta(hv)_1 + \Delta(hv)_2 + \Delta(hv)_3 + \Delta(hv)_4 \\ \Delta z_{b_{2\times 2}} &= \Delta z_{b_1} + \Delta z_{b_2} + \Delta z_{b_3} + \Delta z_{b_4} \end{aligned} \tag{25}$$

where subscripts 1, 2, 3 and 4 denote the fine mesh control volumes. The changes of the flow properties at the fine grid points are calculated,

$$\begin{aligned}
\Delta h_1^{\text{new}} &= \Delta h_1 + I_{2\times2}^{\text{fine}} \Delta h_{2\times2} \\
\Delta (hu)_1^{\text{new}} &= \Delta (hu)_1 + I_{2\times2}^{\text{fine}} \Delta (hu)_{2\times2} \\
\Delta (hv)_1^{\text{new}} &= \Delta (hv)_1 + I_{2\times2}^{\text{fine}} \Delta (hv)_{2\times2} \\
\Delta z_{\text{b}_1}^{\text{new}} &= \Delta z_{\text{b}_1} + I_{2\times2}^{\text{fine}} \Delta z_{\text{b}_{2\times2}}
\end{aligned} \tag{26}$$

where $I_{2\times2}^{\text{fine}}$ is a linear interpolation operator. In general form, a typical relation for this operator is,

$$I_{\text{IMG,JMG}}^{\text{fine}} = \frac{1}{(\text{IMG}+1)(\text{JMG}+1)} \tag{27}$$

Calculations using Equation (26) are repeated for the remaining finite-volumes 2, 3 and 4 of the block under consideration. With the multi-grid approach the use of blocks minimizes the computational work needed to propagate the unsteady waves out of the computational domain so that a steady state is rapidly reached. The optimum convergence of the proposed multi-grid method is typically three times faster than a single grid convergence. A 3×3 multi-grid block was found to be an optimum choice for nearly all currently tested cases. The described multi-grid procedure is easily applied and requires minimal programming effort. One does not need to create coarse grids by, say, removing every other line in the fine mesh. Figure 3 shows the comparisons for the convergence rates for the multi-grid and single grid techniques using a 60×244 points mesh. Detailed description of the flow problem is given in Section 5.2. The single-grid method, after 500 iterations, did not advance the solution below 10^{-4} per cent. The 3×3 multi-grid block scheme achieved convergence after 285 iterations.

4.4. Boundary and initial flow conditions

Hydrodynamic boundaries. There are two flow types of boundary conditions that have to be satisfied: (a) the open boundaries and (b) the solid boundaries. For subcritical flow entrance at the upstream boundary a fixed value of the flow rate and a relative flow direction are specified. At the downstream boundary, uniform across the width, water depth is specified. For supercritical flow entrance, at the upstream boundary the transverse flow velocity component and a uniform across the width water depth are specified along with the total available head. At the downstream boundary all flow physical quantities are left free to change. All required values are extrapolated from the interior grid nodes. To close the problem, the condition of no water mass flow across the solid boundaries needs to be applied. The fluxes hV are set equal to zero across the face of the solid boundary finite-volume (easy implementation). The above conditions proved to be satisfactory for either inviscid or viscous flow calculations.

Sediment transport and bed elevation boundaries. The application of upstream and downstream sediment transport boundaries depends upon the particular application. The condition of no sediment mass flow across the solid boundaries needs also to be applied. In this case the fluxes $Q_{s\eta}$ are set equal to zero across the face of the solid boundary finite-volume. An

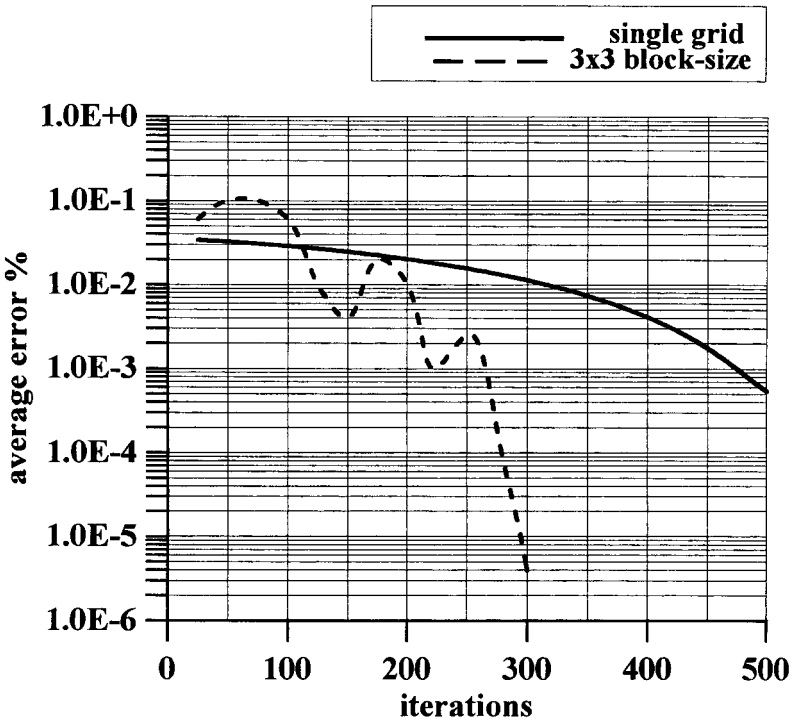

Figure 3. Convergence histories for the Rouse *et al.* [18] channel.

assumption was made that the sediment is to be transported mainly as bed load. Appropriate sediment boundary conditions are applied for each test case. Similarly, up- and downstream bed elevation changes need to be properly applied.

Initial flow conditions. To start the unsteady state computations, the values of three hydrodynamic primary variables, h, hu and hv at time $= 0$ must be specified at all the grid points. Also, the initial topography must be specified.

5. COMPUTATIONAL RESULTS AND DISCUSSION

The proposed numerical method for the calculation of viscous, two-dimensional bed morphology was first tested to predict purely hydrodynamic two-dimensional subcritical and supercritical flow problems. Second, the sediment transport equation was fully coupled and one-dimensional bed morphology problem was tested. Finally, the proposed numerical scheme was tested to predict the bed morphology around abutments using two-dimensional flow analysis. In all tested cases the computed results were validated against measurements and/or other numerical methods available data.

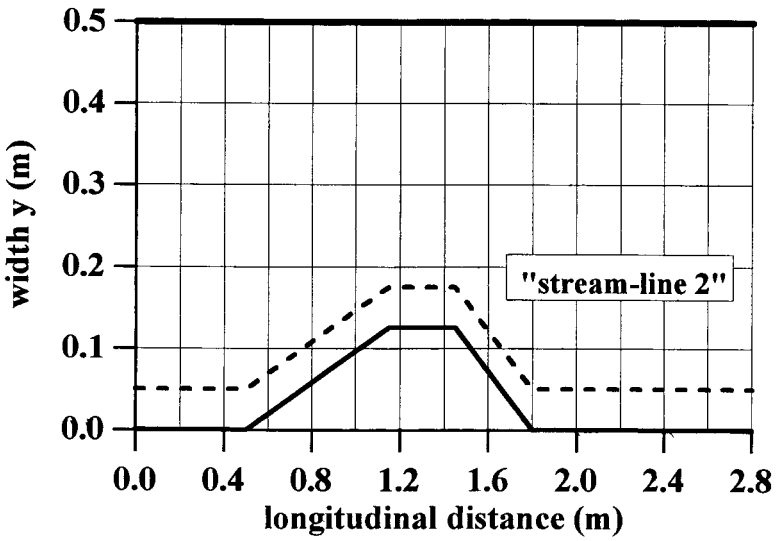

Figure 4. Converging–diverging flume geometry with 'streamlines'.

5.1. *Subcritical flow in a linearly converging–diverging flume*

To investigate the prediction of the proposed numerical scheme it was decided to test it for subcritical flow in a linearly converging–diverging laboratory flume; see Figure 4. The side wall contraction angle is 10.88° giving rise to a relatively high value for $[(\partial b)/(\partial x)] = -0.192$ where b is the channel width. The expansion angle is equal to 21.037° giving rise to $[(\partial b)/(\partial x)] = 0.384$. A value for the Chezy flow friction coefficient C was estimated to be 120.0. It agrees with published values for a glass sided-iron bed flume. Experiments were conducted by Soulis *et al.* [16] along various 'streamlines', throughout the flow field using different discharges, water depths and bottom slopes. Figures 5 and 6 show the comparison along the flume 'streamline 2', located 0.05 m away from the lower side wall (Figure 4), between current method predictions and measured flow for velocity and water depth, respectively, at $Q = 20.58 \times 10^{-3}\ \mathrm{m^3\,s^{-1}}$ with zero slopes in either directions. The predictions of a bi-diagonal implicit numerical scheme developed by Panagiotopoulos and Soulis [17] are also shown. The diverging part of the flume is a high viscous flow region with flow separation and reversal. Maximum axial velocity predicted values are in the $0.56\ \mathrm{m\,s^{-1}}$ region and compare well with measured ones. The comparison between predictions and measurements for depths and velocities is satisfactory, particularly for the converging part of the flume.

5.2. *Supercritical flow in expansion channel*

The channel expansion, shown in Figure 7, was used to test the accuracy of the proposed method for high entrance Froude number (= 4.0). Rouse *et al.* [18] studied experimentally the above supercritical flow. A 29×61 computational grid was used. The actual channel geometry

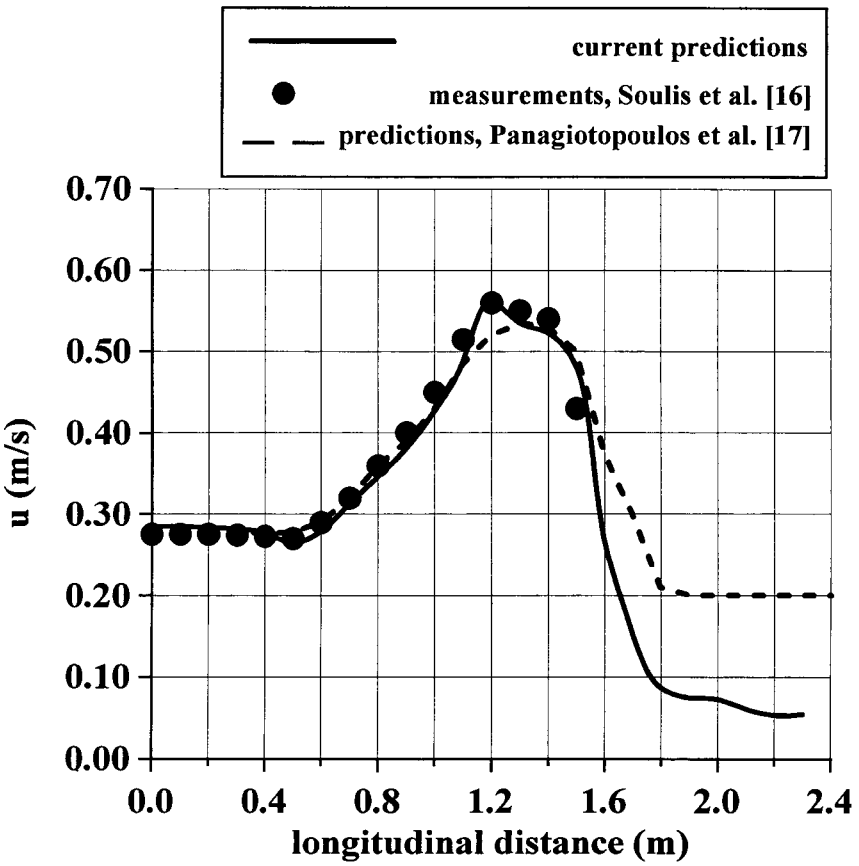

Figure 5. Flow velocity comparison between current method predictions, Panagiotopoulos *et al.* [17] predictions and measurements for the converging–diverging flume along 'streamline 2'at $Q = 20.58 \times 10^{-3}\ \mathrm{m^3\ s^{-1}}$.

is given by the formula,

$$\frac{y}{b_1} = \frac{1}{2}\left(\frac{x}{4.0\,b_1}\right)^{3/2} + \frac{1}{2} \tag{28}$$

where b_1 is the half entrance width. At the upstream end, a constant value of the water depth h_1 equal to 1.0 m is specified. A fixed value of 9.0 m for the total available head is also specified. The Manning's roughness coefficient was set equal to 0.012. Relative depth ratio comparisons between current method predictions using a 29×61 grid, predictions using an implicit bi-diagonal scheme, Panagiotopoulos and Soulis [17] and measurements are shown in Figures 8(a), (b) and (c) for the center line, midstream line (equally distant between curved line and center line), and curved line, respectively. The Froude number is supercritical throughout the flow field. The comparisons are considered to be satisfactory particularly along the midstream flow line. The flow is accelerating and the comparison with measurements is favorable.

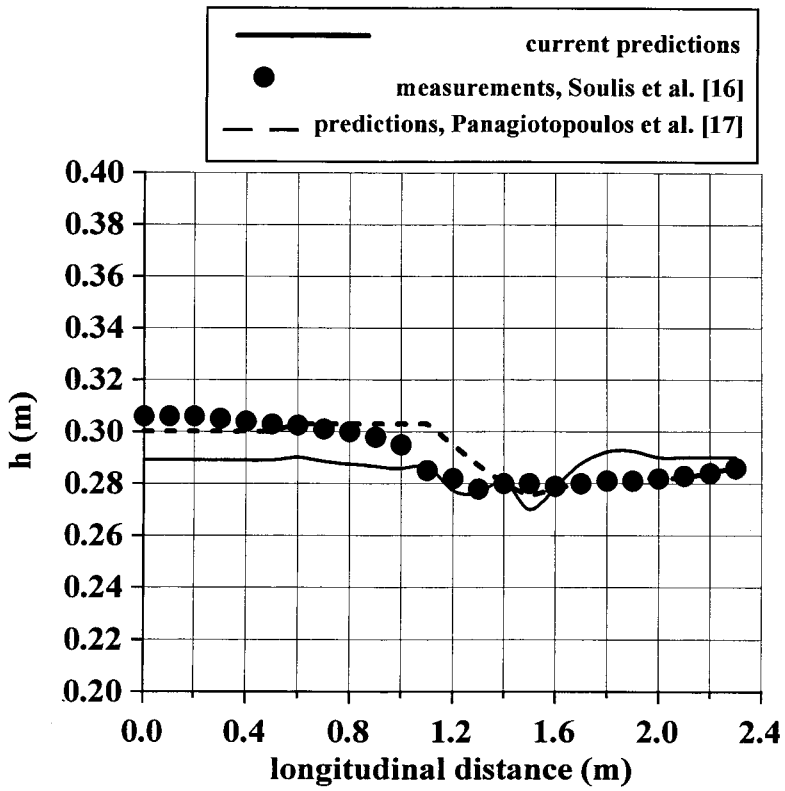

Figure 6. Water depth comparison between current method predictions, Panagiotopoulos *et al.* [17] predictions and measurements for the converging–diverging flume along 'streamline 2' at $Q = 20.58 \times 10^{-3}\,\mathrm{m^3\,s^{-1}}$.

5.3. *Aggradation due to sediment overloading*

If the equilibrium between water and sediment discharge is disturbed by increasing the sediment supply rate that enters the flow, then the aggradation process may take place. The water flow is not able to carry away the excessive sediment quantity deposited on the bed, changing the bed slope. Soni *et al.* [11] used a laboratory flume 0.2-m wide and 30.0-m long to study the bed formation. The bed material consisted of sand with a mean diameter of 0.32 mm. The Manning's roughness coefficient n was estimated to be 0.022 and the porosity p of the sediment bed layer was equal to 0.4. The channel was carrying an initial uniform unit flow discharge q_0 of $0.02\,\mathrm{m^2\,s^{-1}}$ at a uniform flow depth h_0 of 0.05 m. The initial bed slope S_0 was equal to 3.56×10^{-3}. The sediment discharge per unit width was predicted by the empirical power function,

$$q_{sx} = \alpha u^{\beta} \tag{29}$$

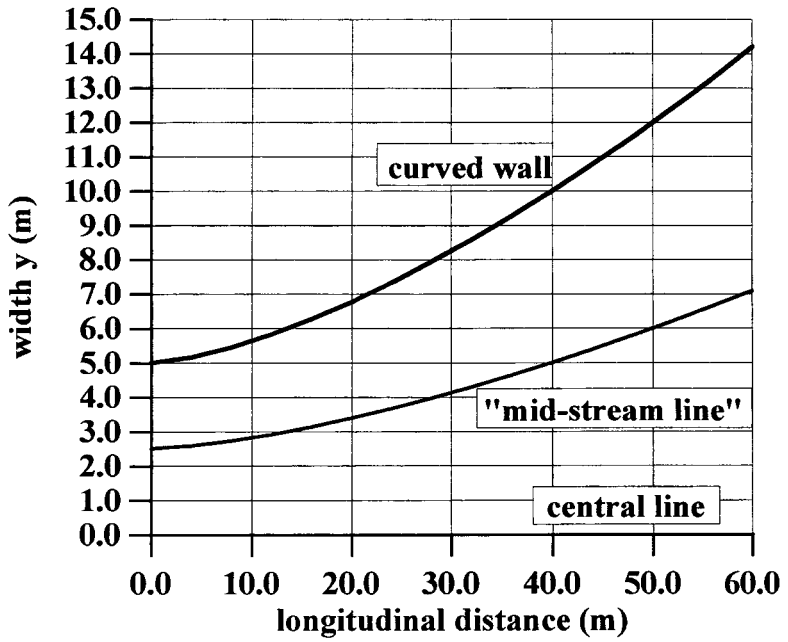

Figure 7. Expansion channel geometry for $Fr_1 = 4.0$ after Rouse *et al.* [18].

where α and β are empirical constants with values 1.45×10^{-3} and 5.0, respectively. The sediment discharge entering the channel at the upstream end is given as,

$$\Delta q_{sx} = 4.0 q_{sx0} \tag{30}$$

where q_{sx0} is the initial sediment discharge per unit width and Δq_{sx} is the increment of the sediment discharge.

A spatial step Δx of 1.0 m and 30 reaches were used. The time step Δt was specified according to Courant–Friedrichs–Lewy (CFL) criterion. The flow was subcritical. At the upstream end a constant water discharge $q(0,t) = q_0$ for all $t \geqslant 0$ was applied while the sediment discharge $q_{sx}(0,t)$ was set equal to Δq_{sx} for all $t \geqslant 0$. The inlet bed elevation at any time is calculated,

$$z_{b_{i,1}} = z_{0_{i,1}} + \frac{\Delta t}{\Delta x_{i,1}(1-p)}(q_{sx_{i,1}} - q_{sx_{i,2}}) \tag{31}$$

$z_{0i,1}$ is the initial bed elevation for the current time step. At the downstream end a constant value for water depth $h(L,t) = h_0$ was specified and the bed elevation was set according to $z_b(L,t) = z_{b0}$, where L is the total length of the flume. Figures 9 and 10 show the comparison between current method predictions, Klonidis and Soulis [7] numerical method predictions and measurements of water depths and bed elevations respectively, after 2400 s.The comparisons are satisfactory. After 2400 s, aggradation takes place from inlet down to 15.0 m longitudinal distance of the tested flume. This process is also well predicted.

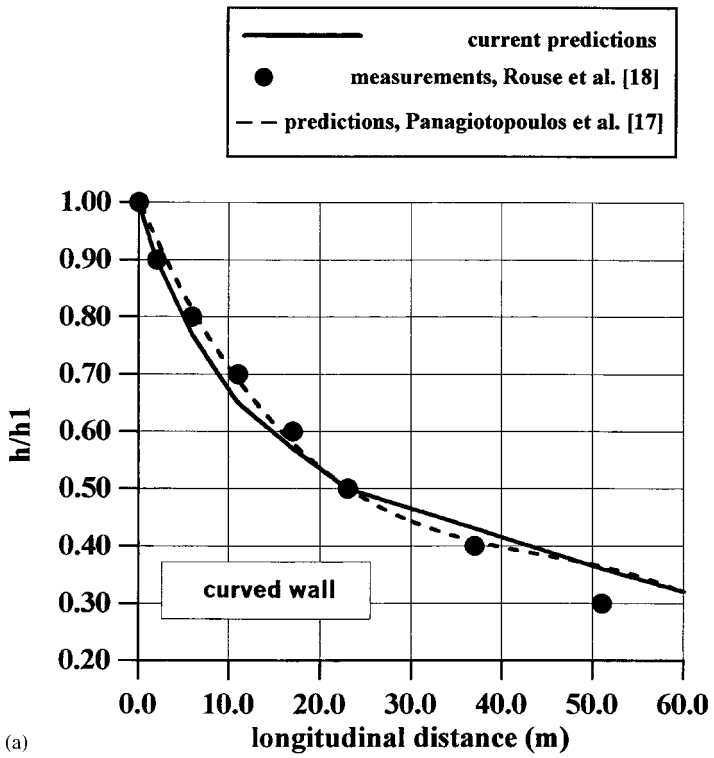

(a)

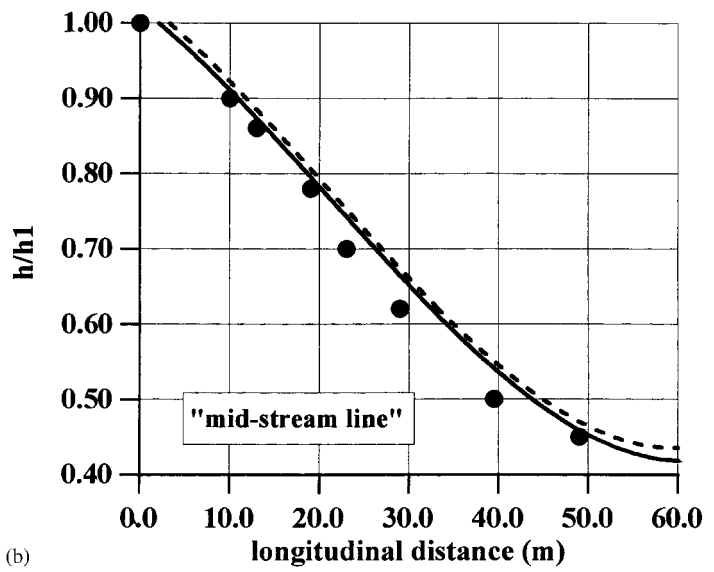

(b)

Figure 8. Water depth comparisons between current method predictions, Panagiotopoulos *et al.* [17] predictions and measurements along (a) curved wall, (b) 'mid-stream line' and (c) central line, for the Rouse *et al.* [18] channel at $Fr_1 = 4.0$, $S_{0x} = 0.0$, $S_{0y} = 0.0$.

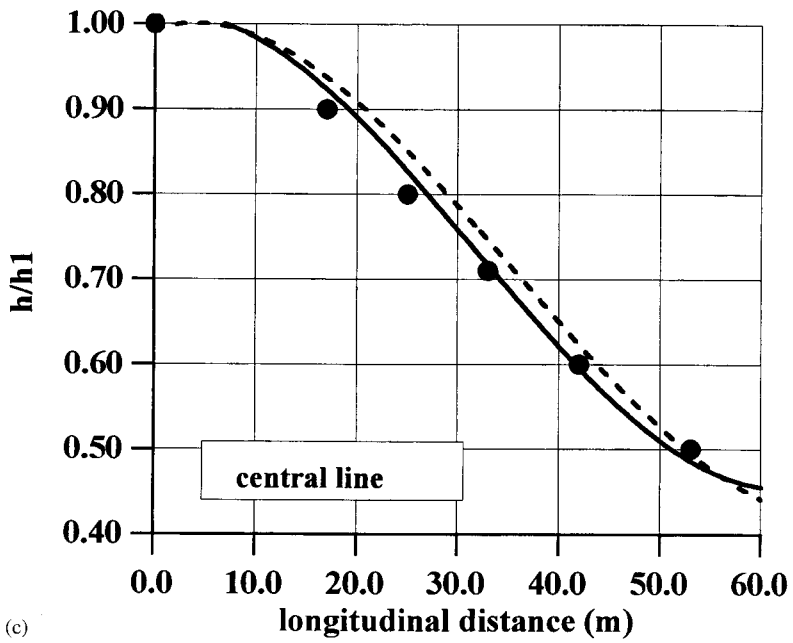

Figure 8. *Continued.*

5.4. Local scour around abutments

Local scour around abutments results from flow disturbances introduced by the presence of the structure. Abutments projecting into a water system produce deep scour holes upstream of the contraction. Experiments were conducted by Farsirotou [19]. She used a sediment flume facility 3.0-m long and 1.50-m wide; see Figure 11. A symmetrical trapezoidal geometry abutment was placed at one side of the flume. The abutment length at its base was equal to 0.50 m while the small base length was 0.10 m and the height is set equal to 0.20 m. The bed was uniformly covered with material consisting of metallurgical coal having a mean grain size D_{50} of 1.10 mm and a specific weight S_g of 1.31, while the depth of the covering material was set equal to 0.10 m. The Manning's roughness coefficient n was estimated to be 0.022 and the porosity p of the sediment bed layer was 0.4. The channel was carrying an initial uniform flow discharge of $0.050\,\mathrm{m^3\,s^{-1}}$ with a uniform flow depth h_0 of 0.08 m. The slope of the flume bed was set equal to zero. There was no sediment discharge entering the channel at the upstream end while at the downstream end the bed elevation was free to change. The applied flow and geometry conditions resulted in subcritical flow throughout the tested flume. A constant value of water depth $h(L,t)=h_0$ at the downstream end was set for all $t \geqslant 0$. Profiles of bed surface elevation were measured at regular time intervals in order to follow the system evolution.

The numerical results obtained from a finite-volume scheme increase in accuracy as the grid spacing is decreased. It is desirable to increase grid resolution in regions where the flow variables exhibit large gradients. Thus, for the abutment problem, the area around it and

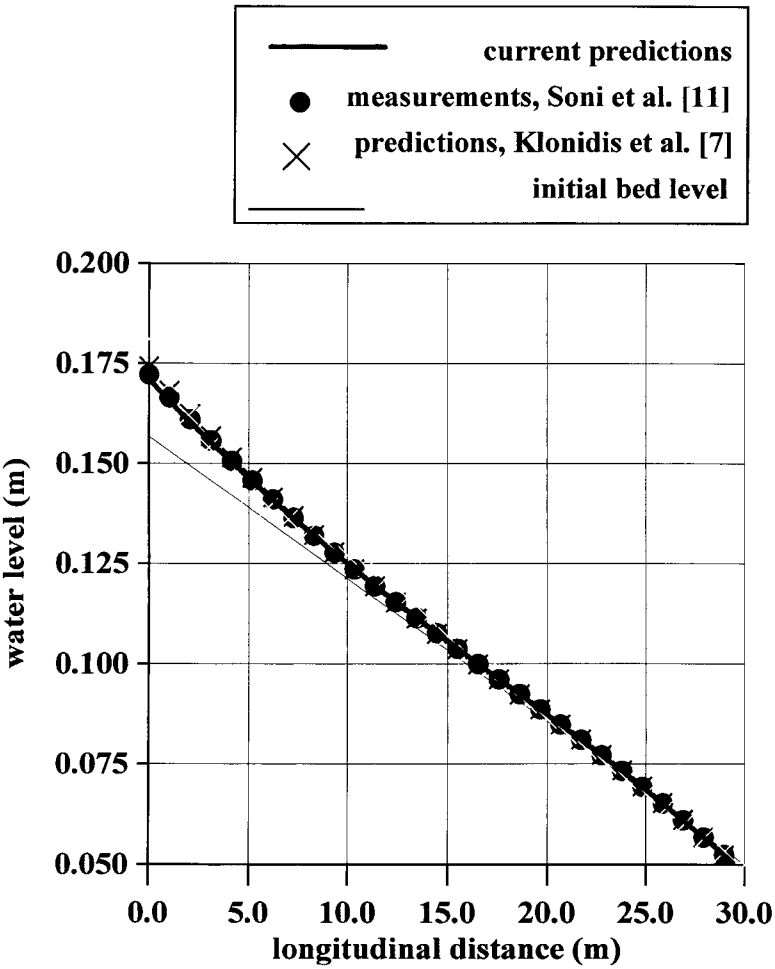

Figure 9. Comparison between computed and measured water level for the Soni *et al.* [11] test case after $t = 2400$ s.

downstream to the abutment zone qualify as high-gradient regions. Henceforth, the grid was dense in this zone.

The inlet bed elevation $z_{bi,1}$ is updated at each iteration from the nearest points according to $z_{b_{i,1}} = 2.0z_{b_{i,2}} - z_{b_{i,3}}$ while the outlet bed elevation $z_{bi,jm}$ is also updated at each iteration from $z_{b_{i,jm}} = 2.0z_{b_{i,jm-1}} - z_{b_{i,jm-2}}$.

In the current application the unit sediment discharges q_{sx} and q_{sy} were predicted using the empirical relation developed by Engelund and Hansen [13],

$$q_{sx} = \frac{uC_b h}{pS_g} \quad \text{and} \quad q_{sy} = q_{sx}\frac{v}{u} \tag{32}$$

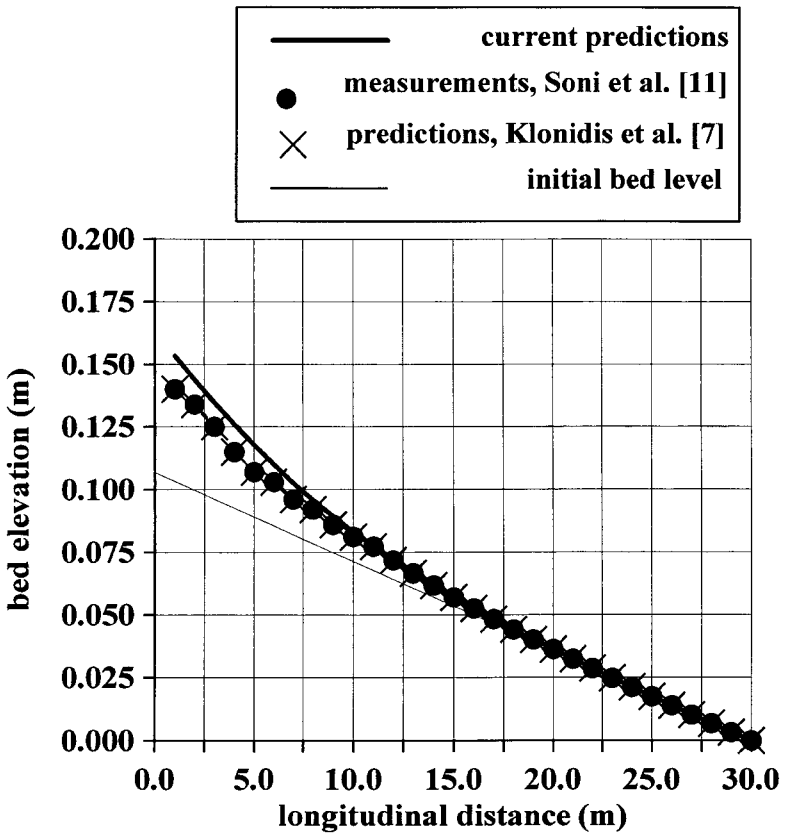

Figure 10. Comparison between computed and measured bed elevation for the Soni *et al.* [11] test case after $t = 2400$ s.

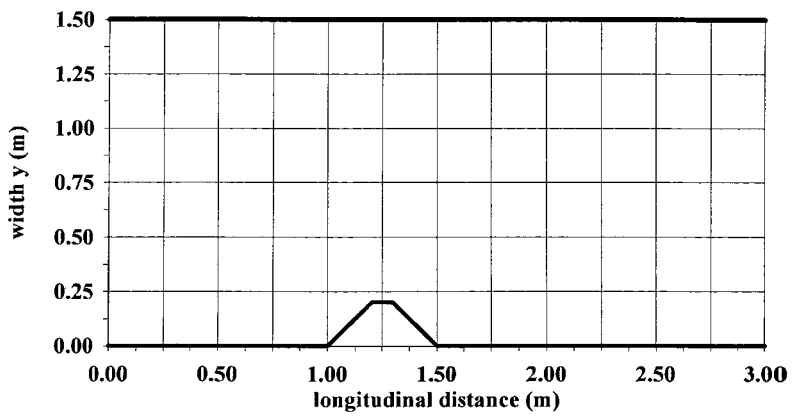

Figure 11. Abutment geometry.

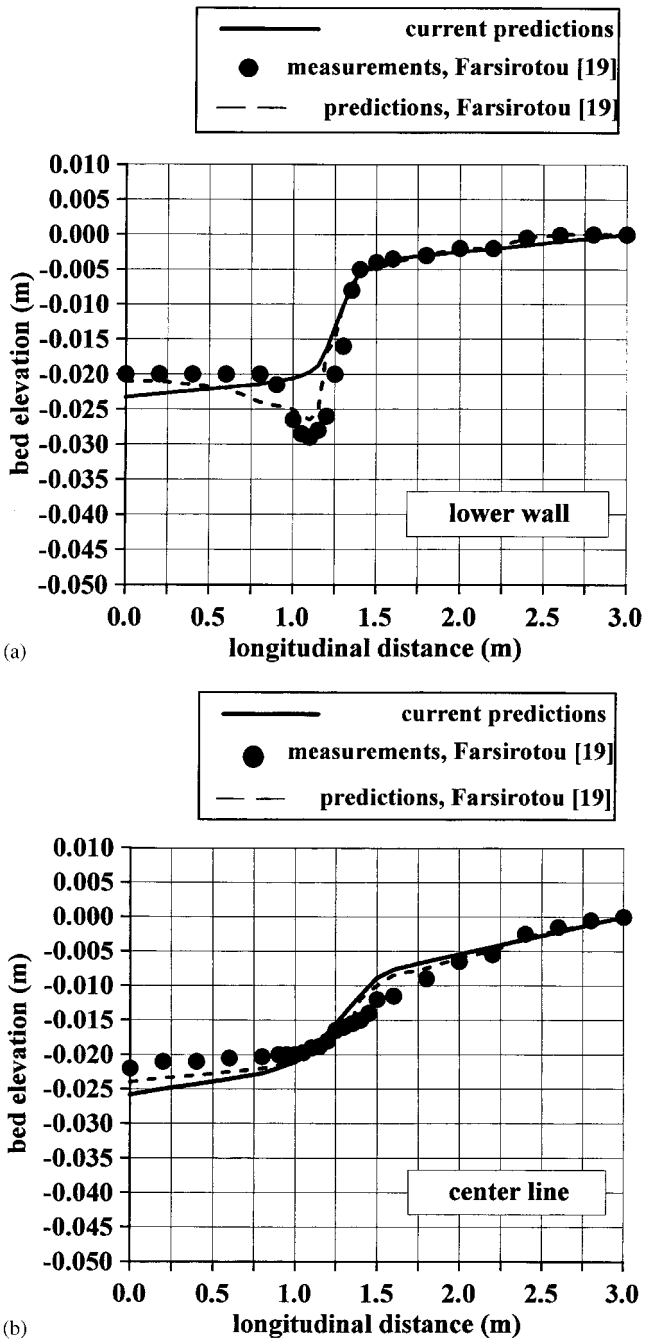

Figure 12. Comparison between current method predictions, Farsirotou [19] predictions and measurements of bed level along the (a) lower wall, (b) center line and (c) upper wall for the abutment at $Q = 0.05\ \mathrm{m}^3\ \mathrm{s}^{-1}$ and $h_2 = 0.08\ \mathrm{m}$ after $t = 300\ \mathrm{s}$.

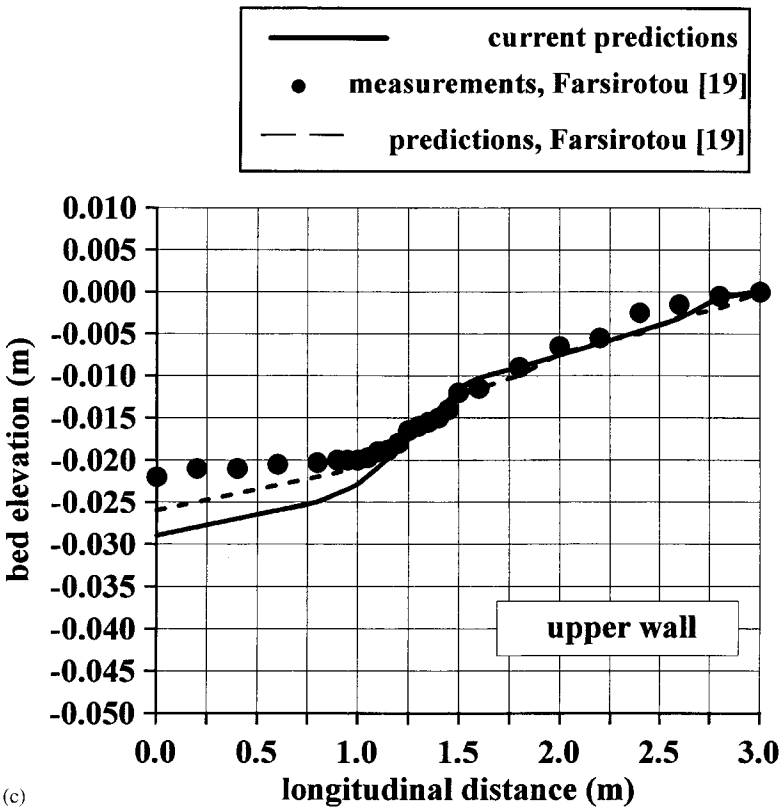

(c)

Figure 12. *Continued.*

where C_b is the sediment concentration given by,

$$C_b = \frac{50 S_g (u^2 + v^2)^{1/2} u_*^3}{h g^2 D_{50} (S_g - 1)^2} \tag{33}$$

with $u_* = \sqrt{gh(S_{fx}^2 + S_{fy}^2)^{1/2}}$ being the shear velocity. The effective kinematic viscosity was calculated using Equation (4). Direct comparisons between current method predictions and measurements after Farsirotou [19] are shown in Figures 12, 13 and 14 along the upper wall (flat wall), the center line (equally distant between upper and lower walls) and the lower wall (abutment), after $t = 300, 600$ and 900.0 s, respectively. The results of an integral, fully coupled numerical method (Farsirotou [19]) are also shown. It must be pointed out that even if the intensity of scour and deposition are different for different values of the parameters the process is qualitatively similar. Due to strong flow acceleration close to the abutment, maximum scour occurs close to the latter. Downstream flow still accelerates, although more slowly, until the contracted section of the abutment is reached. Erosion is mostly concentrated in this region, while smaller scouring is found in the zone where the vortex sheet develops

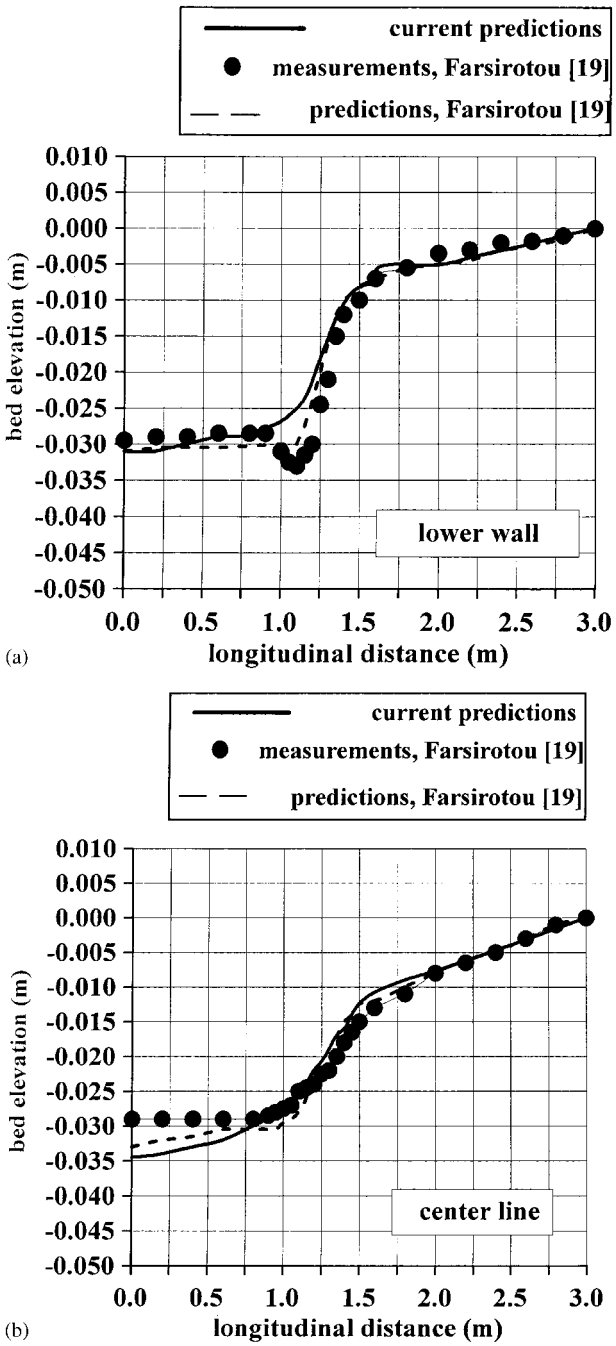

Figure 13. Comparison between current method predictions, Farsirotou [19] predictions and measurements of bed level along the (a) lower wall, (b) center line and (c) upper wall for the abutment at $Q = 0.05\ \mathrm{m^3\ s^{-1}}$ and $h_2 = 0.08\ \mathrm{m}$ after $t = 600\ \mathrm{s}$.

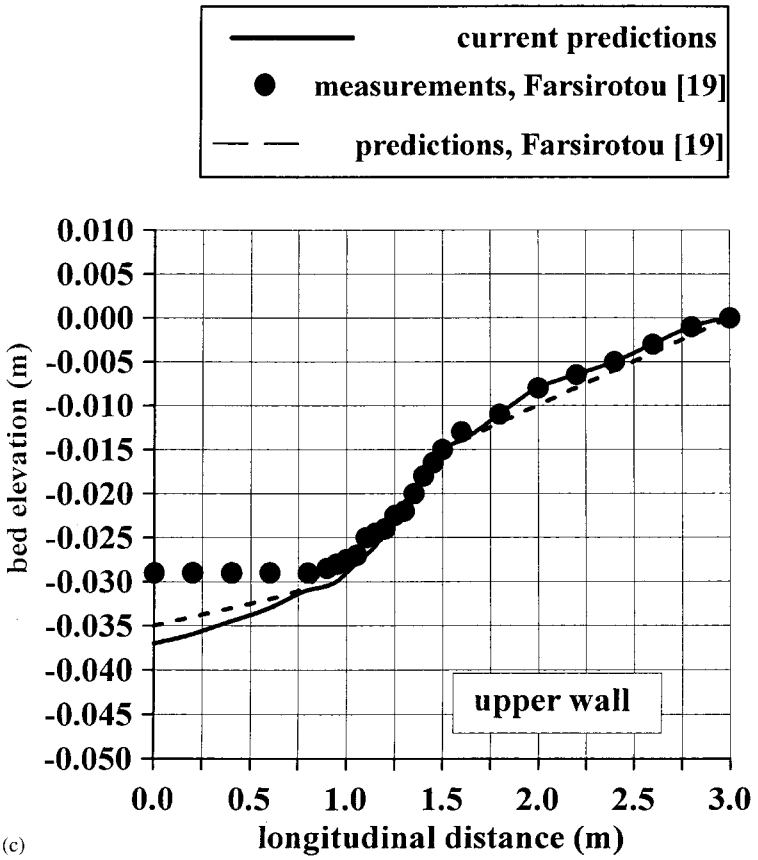

(c)

Figure 13. *Continued.*

(downstream of the contracted section). Minimum measured scour depths in the region 1.0 –1.3 m along the abutment are under-predicted by the current method. However, upstream to the abutment the predictions overestimate the scour depth. This is the rule for all time results. Taking into account the fact that three-dimensional effects must play some role in the actual experimental configuration, the comparison between measurements and computations is reasonably satisfactory, though Farsirotou [19] predictions seem to predict better the measurements in particular abutment regions. In general, the computed results back each other.

6. CONCLUSIONS

A viscous, two-dimensional, fully coupled, finite volume, multi-grid, explicit numerical scheme was developed to solve time-dependent bed deformation in alluvial channels using a transformed computational grid. The numerical technique itself turned out to be flexible concerning its response to handle rapid changes of sediment transport at the boundaries. Also, the proposed

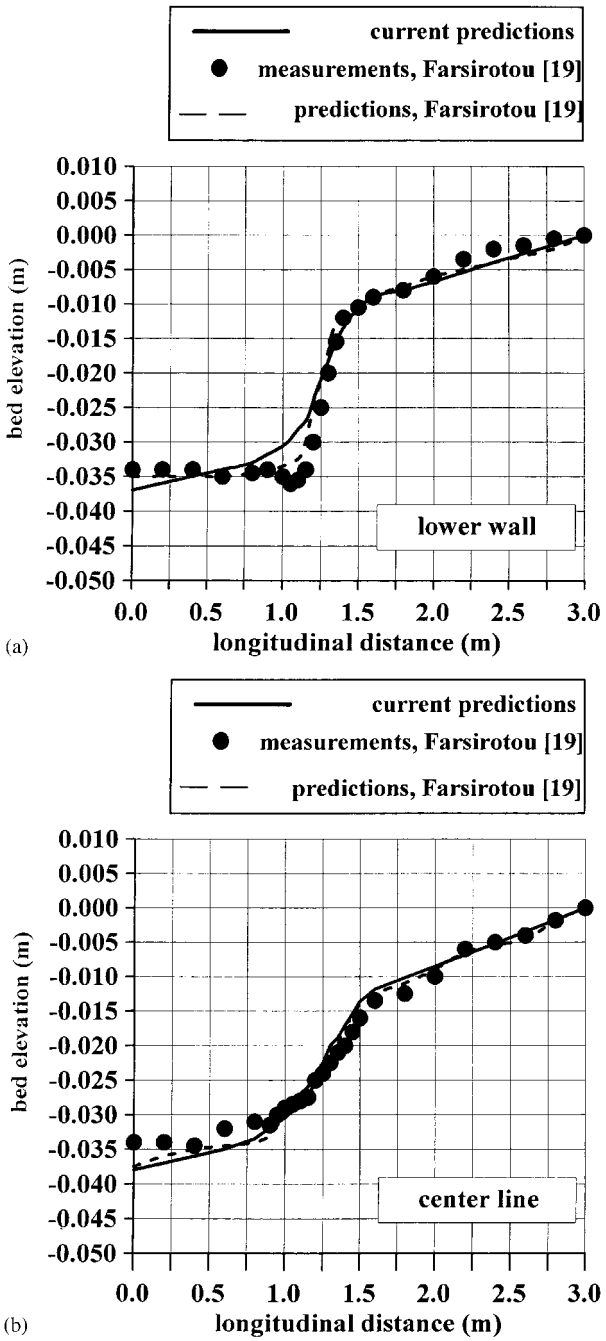

Figure 14. Comparison between current method predictions, Farsirotou [19] predictions and measurements of bed level along the (a) lower wall, (b) center line and (c) upper wall for the abutment at $Q = 0.05\ \mathrm{m}^3\ \mathrm{s}^{-1}$ and $h_2 = 0.08\ \mathrm{m}$ after $t = 900\ \mathrm{s}$.

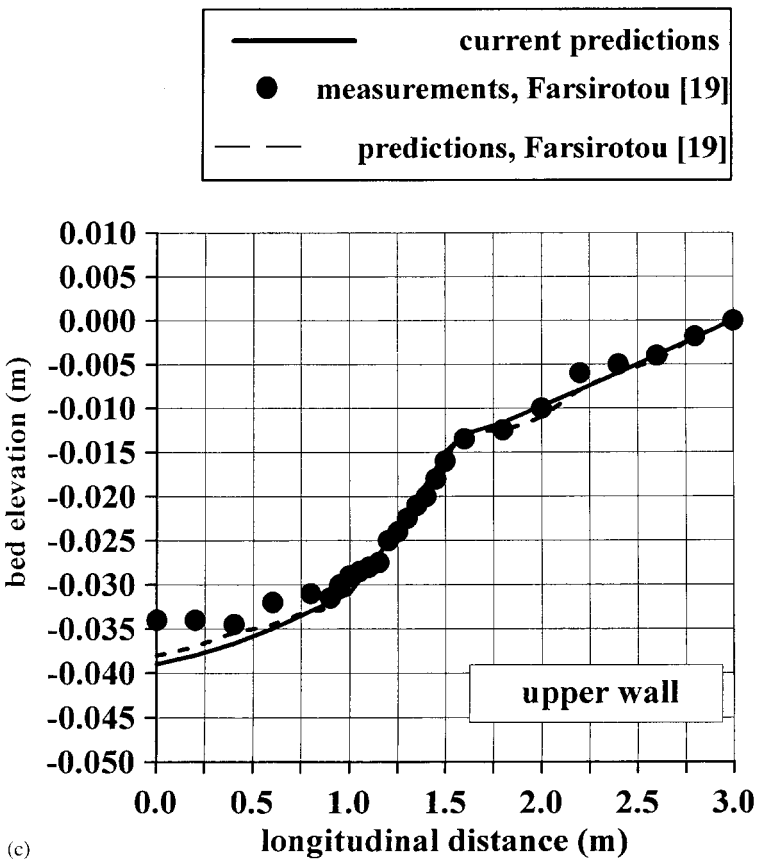

(c)

Figure 14. *Continued.*

model is straightforward to perform on the computer and can include the detailed geometry of the river channel. The agreement between predictions with measurements is satisfactory. Particularly, for the abutment test case reasonable agreement between measured and computed bed elevations near to the abutment flow region has been demonstrated. The applied numerical technique directly (fully) coupling hydrodynamic and bed morphology equations proved to be computationally time consuming. The proposed method is stable, reliable and accurate although time consuming, handling a variety of sediment transport equations.

APPENDIX A. NOMENCLATURE

The following characters and symbols are used in this paper:

Latin

C = Chezy's flow friction coefficient
C_b = sediment concentration

C_1, C_2 = constants
D_{50} = median sediment grain size
FT = time constant
g = acceleration due to gravity
h = flow depth
J = Jacobian
L = total length of flume
n = Manning's flow friction coefficient
p = sediment porosity
$Q_{s\xi}, Q_{s\eta}$ = unit bed load sediment transport in ξ- and η-directions, respectively
q_{sx}, q_{sy} = unit bed load sediment transport in x- and y-directions, respectively
S_{fx}, S_{fy} = friction slopes in x- and y-directions, respectively
S_{m_ξ}, S_{m_η} = smoothing factors in x- and y-directions, respectively
S_g = specific weight
S_{0x}, S_{0y} = channel slopes in x- and y-directions, respectively
t = time
U, V = depth-averaged velocity components in ξ- and η-directions
u, v = depth-averaged velocity components in x- and y-directions
u_* = shear velocity
x, y = Cartesian coordinates, longitudinal and transverse, respectively
z_b = bed elevation

Greek

α, β = constants for empirical power function
H = transformation matrix
$I_{2\times2}^{\text{fine}}$ = interpolation operator
ν_{eff} = effective kinematic viscosity
ξ, η = local coordinates

Symbol

$_1$ = inlet flow conditions
$_2$ = outlet flow conditions

REFERENCES

1. Roulund A, Sumer BM, Fredsoe J. 3D mathematical modelling of scour around a circular pile in current. In *River Sedimentation*, Jayawarden, Lee and Wang (eds). Balkema: Rotterdam, 1999; 131–137.
2. Olsen NRB, Melaaen MC. Three-dimensional calculation of scour around cylinders. *J. Hydr. Engrg., ASCE* 1993; **119**(9):1048–1054.
3. Richardson E, Panchang VG. Three-dimensional simulation of scour-inducing flow at bridge piers. *J. Hydr. Engrg., ASCE* 1998; **124**(5):530–540.
4. Struiksma N, Olsen KW, Flokstra C, De Vriend HJ. Bed deformation in curved alluvial channels. *J. Hydr. Res.* 1985; **23**(11):57–79.
5. Kassem AA, Chaudhry MH. Comparison of coupled and semi-coupled numerical models for alluvial channels. *J. Hydr. Engrg., ASCE* 1998; **124**(8):794–802.
6. Bhallamudi SM, Chaudhry MH. Numerical modeling of aggradation and degradation in alluvial channels. *J. Hydr. Engrg., ASCE* 1991; **117**(9):1145–1164.
7. Klonidis AJ, Soulis JV. An implicit numerical scheme for bed morphology calculations. In *VII Int. Conference Computational Methods and Experimental Measurements VIII.* Computational Mechanics Publications: Rhodes, Greece, 1997; 381–390.

8. Farsirotou ED, Soulis JV, Dermissis VD. A numerical algorithm for bed morphology equations. In *Int. Conference European River Development.* Budapest, Hungary, 1998.
9. De Vries JW, Klaasen GJ, Struiksma N. On the use of movable bed models for river problems: state of the art. *Symp. River Sedimentation.* Beijing, China, 1989.
10. Soulis JV. Multiple grid solution of the open channel flow equations using a marching finite-volume method. *Adv. Water Resources* 1991; **14**(4):203–214.
11. Soni JP, Garde RJ, Raju KG. Aggradation in streams due to overloading. *J. Hydr. Engrg.*, *ASCE* 1980; **106**(1):117–132.
12. Ackers P, White WR. Sediment transport: a new approach and analysis. *Proc. ASCE* 1973; **99**(HY 11): 2041–2060.
13. Engelund F, Hansen E. *A Monograph on Sediment Transport in Alluvial Streams*. Teknish Vorlag: Copenhagen, 1967.
14. Brownlie WR. Flow depth in sand bed channels. *J. Hydr. Engrg.*, *ASCE* 1983; **109**(7).
15. Smart GM. Sediment transport formula for steep channels. *J. Hydr. Engrg.*, *ASCE* 1984; **110**(3):267–276.
16. Soulis JV, Alexiou EE, Kounavas EK. Measurements and computations of non-uniform flow. *Tech. Chron.- A* 1991; **11**(2).
17. Panagiotopoulos AG, Soulis JV. A bidiagonal scheme for depth-averaged free-surface flow equations. *J. Hydr. Engrg.*, *ASCE* 2000; **126**(6):425–437.
18. Rouse H, Bhoota BV, Hsu EY. Design of channel expansions. *Transactions ASCE* 1951; **116**:347–363.
19. Farsirotou ED. A numerical and experimental study of scouring and deposition in alluvial channel. *Ph.D. Thesis* (*in Greek*), *Civil Engineering Department, Aristotelion University of Thessaloniki*, Thessaloniki, Greece, 1999.

